AGU PUBLICATIONS

JGR

Journal of Geophysical Research: Atmospheres

RESEARCH ARTICLE
10.1002/2015JD024529

Key Points:
- Large eddies cause flux divergence/convergence in the atmospheric surface layer
- Large eddies modulate turbulence structure and fluxes
- Large eddies can either improve or degrade the surface energy balance closure

Correspondence to:
H. Liu,
heping.liu@wsu.edu

Citation:
Gao, Z., H. Liu, E. S. Russell, J. Huang, T. Foken, and S. P. Oncley (2016), Large eddies modulating flux convergence and divergence in a disturbed unstable atmospheric surface layer, *J. Geophys. Res. Atmos.*, *121*, 1475–1492, doi:10.1002/2015JD024529.

Received 20 NOV 2015
Accepted 20 JAN 2016
Accepted article online 22 JAN 2016
Published online 18 FEB 2016

Large eddies modulating flux convergence and divergence in a disturbed unstable atmospheric surface layer

Zhongming Gao[1], Heping Liu[1], Eric S. Russell[1], Jianping Huang[2], Thomas Foken[3], and Steven P. Oncley[4]

[1]Laboratory for Atmospheric Research, Department of Civil and Environmental Engineering, Washington State University, Pullman, Washington, USA, [2]Key Laboratory for Semi-Arid Climate Change of the Ministry of Education, College of Atmospheric Sciences, Lanzhou University, Lanzhou, China, [3]Bayreuth Center of Ecology and Environmental Research, University of Bayreuth, Bayreuth, Germany, [4]National Center for Atmospheric Research/EOL, Boulder, Colorado, USA

Abstract The effects of large eddies on turbulence structures and flux transport were studied using data collected over a flat cotton field during the Energy Balance Experiment 2000 in the San Joaquin Valley of California in August 2000. Flux convergence (FC; larger fluxes at 8.7 m than 2.7 m) and divergence (FD) in latent heat flux (LE) were observed in a disturbed, unstable atmospheric surface layer, and their magnitudes largely departed from the prediction of Monin-Obukhov similarity theory. From our wavelet analysis, it was identified that large eddies affected turbulence structures, scalar distribution, and flux transport differently at 8.7 m and 2.7 m under the FC and FD conditions. Using the ensemble empirical mode decomposition, time series data were decomposed into large eddies and small-scale background turbulence, the time-domain characteristics of large eddies were examined, and the flux contribution by large eddies was also determined quantitatively. The results suggest that large eddies over the frequency range of $0.002\ \mathrm{Hz} < f < 0.02\ \mathrm{Hz}$ (predominantly 300–400 m) enhanced the vertical velocity spectra more significantly at 8.7 m than 2.7 m, leading to an increased magnitude of the cospectra and thus LE at 8.7 m. In the FD case, however, these large eddies were not present and even suppressed in the vertical velocity spectra at 8.7 m. Consequently, the cospectra divergence over the low-frequency ranges primarily caused the LE divergence. This work implies that large eddies may either improve or degrade the surface energy balance closure by increasing or decreasing turbulent fluxes, respectively.

1. Introduction

Turbulent transport of momentum, heat, water vapor, and trace gases is an important research subject in the atmospheric surface layer (ASL). Many of the measurement techniques and models of turbulent transport in the ASL rely on Monin-Obukhov similarity theory (MOST) [*Monin and Obukhov*, 1954]. Recently, the validity of MOST, which traditionally assumes less than 10% flux convergence and divergence in the ASL [*Stull*, 1988], has been challenged [e.g., *Sun et al.*, 2003; *Foken*, 2006]. Numerous studies have identified several features that are inconsistent with the predictions of MOST [*Andreas*, 1987; *McNaughton and Laubach*, 2000; *Högström et al.*, 2002; *McNaughton and Brunet*, 2002; *McNaughton*, 2004a, 2004b; *Ruppert et al.*, 2006; *Smedman et al.*, 2007; *Zhang et al.*, 2010]. These features include relatively low correlation coefficient γ_{uw} (e.g., −0.3 for near-neutral ASL) for longitudinal (u) and vertical (w) wind velocity ($\gamma_{uw} = \overline{u'w'}/\sigma_u\sigma_w$, where σ_u and σ_w are the standard deviations for u and w, respectively) [e.g., *Kaimal and Finnigan*, 1994], departures of correlation coefficient $\gamma_{\theta q}$ from unity ($\gamma_{\theta q} = \overline{\theta' q'}/\sigma_\theta\sigma_q$, where σ_θ and σ_q are the standard deviations for temperature (θ) and water vapor density (q), respectively) [e.g., *Ruppert et al.*, 2006], the increase of σ_w/u_* (u_* is friction velocity) with height above the ground [e.g., *Högström et al.*, 2002], and the enhancement of the u and v spectra at the low-frequency range [e.g., *McNaughton and Laubach*, 2000; *Zhang et al.*, 2010]. Thus, the departures from MOST were attributed to the disturbance of large-scale coherent eddies (hereafter large eddies) in the ASL [e.g., *McNaughton and Laubach*, 2000; *Högström et al.*, 2002; *Ruppert et al.*, 2006; *Zhang et al.*, 2010].

Previous studies have pointed out that large eddies, which obey outer layer scaling parameters, frequently disturb the ASL, interact with local turbulence structures, and modulate the turbulent transport of momentum, heat, water vapor, and trace gases in the ASL [*McNaughton and Laubach*, 2000; *Högström et al.*, 2002; *McNaughton and Brunet*, 2002; *McNaughton*, 2004a, 2004b; *Smedman et al.*, 2007; *Zhang et al.*, 2010]. Moreover, it is likely that large eddies can partially explain the dissimilarity of turbulent scalar transport. *Ruppert et al.* [2006] found that poor scalar similarity between θ, q, and carbon dioxide could be attributed

primarily to large eddies with frequencies less than 0.01 Hz based on their analysis of scalar correlation coefficients. The origins of large eddies are diverse, including topographically induced motions in the stable ASL [*Andreas*, 1987], horizontal advection because of heterogeneous terrain surface [*Zermeño-Gonzalez and Hipps*, 1997] and detached eddies generated by shearing motions in the neutral ASL [*Högström et al*., 2002], the convective motions in the outer layer of the convective boundary layer (CBL) [*McNaughton and Brunet*, 2002; *Zhang et al*., 2010], attached eddies initiated by instabilities in the ASL [*McNaughton*, 2004a], and secondary circulations generated by heterogeneous terrain [*Foken*, 2008]. However, the contributions of large eddies to the total turbulent exchange and interactions between the large eddies and small-scale turbulence are not yet well understood [*von Randow et al*., 2006; *Zhang et al*., 2010].

Based on the analysis of the Fourier power spectra of the wind velocity components, previous studies have proposed alternative theories to interpret turbulence structures in the disturbed ASL [*Högström et al*., 2002; *McNaughton and Brunet*, 2002; *McNaughton*, 2004b; *Smedman et al*., 2007]. *Högström et al*. [2002] proposed a "top-down" mechanism in which detached eddies, originating from the outer layer, continuously descend and impinge onto the surface, influencing turbulence structures in the ASL. The observation that spectra follow the k^{-1} power laws in the self-similar range (k is wave number) suggests that according to the top-down mechanism, ASL turbulence is subjected to the influence of nonlocal, detached eddies. On the other hand, *McNaughton* [2004b] proposed a "bottom-up" model, termed the Theodorsen ejection amplifier-like model, to categorize turbulence to be a self-organizing ensemble of coherent structures initiated by ejections from the ground. In this bottom-up model, large eddies act as drivers to create shear across the surface, modulating turbulence processes in the ASL. Even though these mechanisms can explain some of the features that depart from MOST [*Hong et al*., 2004; *Smedman et al*., 2007], the ways in which large eddies affect the ASL turbulence and the extent to which large eddies modulate the turbulent transport in the ASL remain unclear [*von Randow et al*., 2006; *Smedman et al*., 2007; *Zhang et al*., 2010].

Besides the Fourier analysis, several methods have been introduced to study the turbulence structures in the ASL, including the Ogive analysis, wavelet analysis, and ensemble empirical mode decomposition (EEMD) [e.g., *Gao and Li*, 1993; *Hudgins et al*., 1993; *Oncley et al*., 1996; *Katul et al*., 2001; *Hong et al*., 2010; *Barnhart et al*., 2012; *Wang et al*., 2013; *Charuchittipan et al*., 2014]. These methods have proven to be effective for research in practice. For example, the wavelet transform of turbulence data provides both scale and time information of the turbulence structures and allows one to separate and sort out different structures with different time scales [*Gao and Li*, 1993]. The empirical mode decomposition (EMD) was proposed to analyze nonstationary and nonlinear data by *Huang et al*. [1998]. Compared with Fourier and wavelet decomposition, EMD is a general data-driven method without any a priori basis functions [*Huang et al*., 1998; *Huang and Wu*, 2008]. It has been applied with success in atmospheric turbulence research [e.g., *Hong et al*., 2010; *Barnhart et al*., 2012; *Wang et al*., 2013].

Flux convergence and divergence in latent heat flux (LE) were observed during the Energy Balance Experiment (EBEX-2000) [*Oncley et al*., 2007]. EBEX-2000 was conducted to investigate the main causes for the surface energy closure problem over a closed canopy with high evapotranspiration [*Mauder et al*., 2007; *Oncley et al*., 2007]. Large LE was attributed to high moist soil that increases the partitioning of available energy into latent heat flux [e.g., *Huang et al*., 2008; *Wang et al*., 2010; *Zhang et al*., 2010]. From analyzing one day's data from EBEX-2000, *Zhang et al*. [2010] attributed the flux convergence and divergence to the frequent disturbances of large eddies which were generated due to the soil moisture heterogeneity in addition to horizontal advection of dry air masses that generated variations in water saturation deficit. However, less is known about the effects of large eddies on turbulence structures and flux transport in the ASL. The objective of this study is to explore how large eddies modulate turbulence structures and flux transport and cause flux convergence and divergence, through detailed analyses of the EBEX-2000 data set using newly developed methods. Section 2 introduces the experiment site, instruments, and the postfield data processing procedures as well as data selection criteria. Section 3 briefly describes the methods used in this study, including wavelet spectral analysis, and ensemble empirical mode decomposition (EEMD). Section 4 presents the results and discussion, and section 5 summarizes conclusions.

2. Experimental Data

2.1. Site Description and Instrumentation

The Energy Balance Experiment (EBEX-2000) was conducted over a cotton field in the San Joaquin Valley, California, USA (Pacific Daylight Time, PDT = UTC—7 h; 36°06'N, 119°56'W; 67 meters above sea level) from

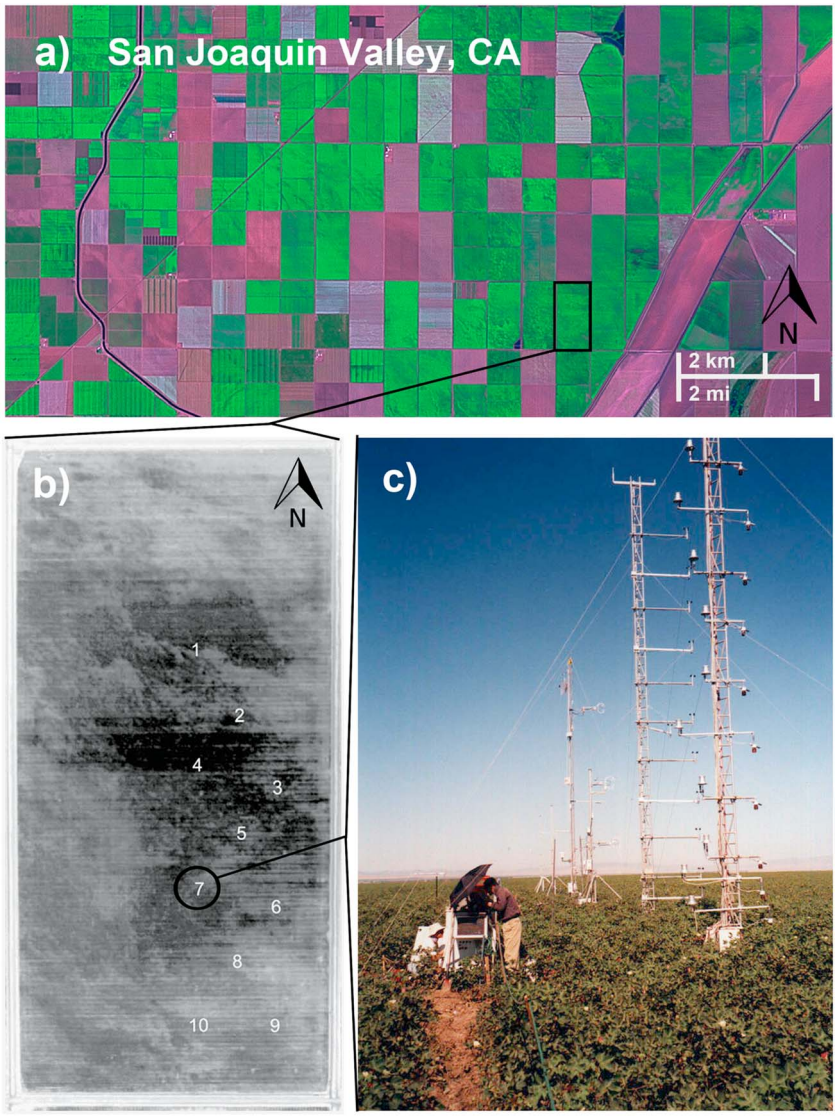

Figure 1. The EBEX-2000 field site: (a) Landsat 7 Enhanced Thematic Mapper Plus image from the United States Geological Survey showing the EBEX-2000 field landscape on 5 August 2000 (http://landsat.usgs.gov/). (b) Near-infrared image of the 1600 × 800 m field with 10 sites locations (adopted from *Oncley et al*. [2007]). (c) Layout of towers in Site 7 with two profile towers in the front and the flux towers in the background.

20 July to 24 August 2000 to determine why observations of terms of the surface energy balance often do not sum to zero [*Oncley et al*., 2007]. The topography of the experimental field was flat and there was a bare dirt field to the north of the cotton field (Figure 1a). Ten tower sites were erected during the field campaign (Figure 1b). The data set analyzed here was collected at Site 7 (Figure 1c). Around the site, the vegetation was uniform with canopy coverage of 90% to 95% and canopy height of 0.9 m. During the field campaign, patch-by-patch irrigation was performed twice from north to south and passed over Site 7 on 2 and 16 August 2000 [*Oncley et al*., 2007], leading to a nonuniform soil moisture regime across the field and horizontal gradients in evapotranspiration. At Site 7, the instruments relevant to our study were two three-dimensional sonic anemometers (CSAT3, Campbell Scientific, Inc.) and two krypton hygrometers (KH20, Campbell Scientific, Inc.) measuring longitudinal, lateral, and vertical wind velocity components (u, v, and w), θ, and q at two heights (8.7 and 2.7 m). These data were sampled at 10 Hz and logged with a datalogger (CR23X, Campbell Scientific Inc.). Other data used here include 30 min averaged net radiation, air pressure, air temperature, and relative humidity obtained from low-response instruments recorded at 1 sample s^{-1}.

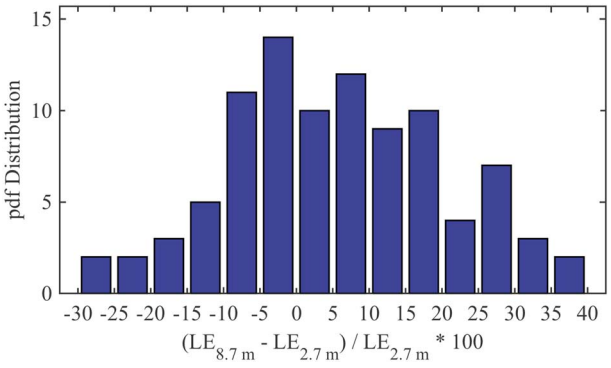

Figure 2. Probability density function (pdf) distribution for the relative difference of latent heat flux (LE) between 8.7 m and 2.7 m.

2.2. Data Processing and Selection

The data processing procedures involved (1) removing physically impossible values and spikes from time series; (2) double rotation for the sonic anemometer wind velocities [*Kaimal and Finnigan*, 1994]; (3) calculation of averages, variances, and covariances using a 30 min block average; (4) sonic temperature correction [*Schotanus et al.*, 1983; *Liu et al.*, 2001], oxygen cross sensitivity correction for KH20 [*Tanner et al.*, 1993], density correction applied to LE [*Webb et al.*, 1980], and correction for flux attenuation due to spatial separation of CSAT3 and KH20 [*Oncley et al.*, 2007]; and (5) quality check for stationary and developed turbulent conditions [*Foken et al.*, 2004]. The primary purpose of this study is to analyze the modulation of turbulent transport by large eddies under unstable conditions. Unstable conditions are defined as data with the Obukhov stability parameter $-1.0 < \zeta < -0.01$ ($\zeta = (z-d)/L$, where z is the measurement height, d is the zero-plane displacement, and L is the Obukhov length). Data also were selected to have (1) the turbulence intensity, I_u ($I_u = \sigma_u/\bar{u}$, where $\bar{u}$ and σ_u are the 30 min mean and standard deviation of u), less than 0.5 to assure Taylor's frozen turbulence hypothesis and (2) net radiation R_n larger than 100 W m^{-2} (the downwelling shortwave radiation was larger than 200 W m^{-2}) to guarantee a well-developed CBL. The data with higher wind speed (>4 m s^{-1}) and with winds from directions between 60° and 300° were excluded to eliminate the effects of unsteady flows and horizontal advection on turbulent transport (about 10% of the data were excluded because of persistent northerly winds during the daytime). Figure 2 shows the probability density function (pdf) distribution for the relative difference of LE between 8.7 m and 2.7 m, $(LE_{8.7\,m} - LE_{2.7\,m})/LE_{2.7\,m} \times 100$, under unstable conditions after the above data selection procedures. In this study, the flux convergence (hereafter FC) is defined when LE at 8.7 m is at least 10% larger than 2.7 m, and flux divergence (hereafter FD) when LE at 8.7 m is at least 10% less than 2.7 m to ensure statistical significance in comparisons. In addition, the difference of greater than 10% in fluxes between two levels in the ASL implies invalidation of MOST [*Stull*, 1988]. The summary of flux and turbulence statistics for the FC group and the FD group (34 and 13 half-hour runs, respectively) under unstable conditions is listed in Table 1. Note that some FC and FD points were excluded because they did not meet the wind direction criteria.

3. Methodology

3.1. Wavelet Analysis

The power spectra of wind velocity and scalars and their cospectra were computed using a continuous wavelet transform (Morlet wavelet) following *Torrence and Compo* [1998]. In contrast to Fourier spectral analysis, the continuous wavelet transform can account for transitions occurring during the observation period (i.e., nonstationary time series) [*Farge*, 1992; *Hudgins et al.*, 1993; *Katul et al.*, 2001]. In addition, the wavelet spectrum provides more detail at lower frequencies while retaining the overall shape at higher frequencies. As demonstrated by *Hudgins et al.* [1993], wavelet analysis offers a better, smoothed global spectral estimate than Fourier power spectra without involving binning and smoothing routines.

The continuous wavelet transform $W_n^x(s)$ of a time series (x_t), with equal time step δt, is defined as the convolution of x_t with a scaled and translated wavelet function ψ_0:

$$W_n^x(s) = \sqrt{\frac{\delta t}{s}} \sum_{t=0}^{N-1} x_t \psi_0^* \left[\frac{(t-n)\delta t}{s} \right], \tag{1}$$

where s is the wavelet scale, n is the localized time index, N is the number of points, (*) denotes the complex conjugate, and $\sqrt{\delta t/s}$ is used to normalize the wavelet function to ensure unit energy at each scale, s.

Table 1. Mean and Standard Deviations of Fluxes and Turbulence Statistics for Flux Convergence (FC: 34 Runs) and Flux Divergence (FD: 13 Runs)[a]

		FC (34 Runs)	FD (13 Runs)
		Mean ± SD	Mean ± SD
LE (W m^{-2})	**8.7 m**	**384.3 ± 107.6**	**259.6 ± 83.8**
	2.7 m	316.9 ± 84.3	317.9 ± 108.0
H (W m^{-2})	**8.7 m**	**44.4 ± 27.7**	**25.1 ± 21.0**
	2.7 m	50.4 ± 23.1	45.7 ± 22.9
u_* (m s^{-1})	**8.7 m**	0.26 ± 0.05	0.23 ± 0.05
	2.7 m	**0.25 ± 0.04**	**0.28 ± 0.04**
ζ	**8.7 m**	−0.29 ± 0.27	−0.22 ± 0.24
	2.7 m	−0.09 ± 0.06	−0.05 ± 0.03
$\bar{u}$ (m s^{-1})	**8.7 m**	2.46 ± 0.52	2.95 ± 0.64
	2.7 m	1.90 ± 0.34	2.19 ± 0.40
σ_u/u_*	**8.7 m**	2.67 ± 0.55	2.47 ± 0.26
	2.7 m	2.60 ± 0.41	2.44 ± 0.12
σ_v/u_*	**8.7 m**	2.79 ± 0.65	2.80 ± 0.81
	2.7 m	2.65 ± 0.50	2.58 ± 0.61
σ_w/u_*	**8.7 m**	**1.44 ± 0.22**	**1.20 ± 0.06**
	2.7 m	1.20 ± 0.09	1.18 ± 0.06
σ_q/Q_*	**8.7 m**	1.86 ± 0.44	1.91 ± 0.40
	2.7 m	2.30 ± 0.36	2.40 ± 0.36
σ_θ/θ_*	**8.7 m**	2.46 ± 0.87	2.73 ± 0.91
	2.7 m	3.18 ± 0.98	3.52 ± 0.97
γ_{uw}	**8.7 m**	**−0.29 ± 0.11**	**−0.23 ± 0.07**
	2.7 m	−0.33 ± 0.07	−0.35 ± 0.02
$\gamma_{\theta q}$	**8.7 m**	**0.67 ± 0.10**	**0.53 ± 0.17**
	2.7 m	0.71 ± 0.06	0.64 ± 0.13

[a]The standard deviations of σ_u, σ_v, σ_w, σ_q, and σ_θ were normalized by u_*, Q_*, and θ_* at 2.7 m. Numbers in bold font indicate statistically significant difference between the FC and FD group at 95% level. SD, standard deviation.

3.2. Ensemble Empirical Mode Decomposition (EEMD)

Using a sifting process, the EMD decomposes a time series, $x(t)$, into a finite number of intrinsic mode functions (IMFs), and an overall residual or trend, $r(t)$,

$$x(t) = r(t) + \sum_{j=1}^{n} \mathrm{IMF}_{j,\,x}(t), \qquad (2)$$

where $\mathrm{IMF}_{j,\,x}$ is the jth IMF for the time series x.

Each IMF represents the oscillation mode embedded in the time series data [*Huang et al.*, 1998]. To eliminate the mode-mixing problem caused by signal intermittency and to extract robust and statistically significant IMFs, ensemble EMD (EEMD) was developed by *Wu and Huang* [2009]. EEMD defines the IMFs as mean of an ensemble of trials of EMD—each consisting of the time series plus injected white noise of known finite amplitude. The Hilbert transform is used to calculate the instantaneous frequency and amplitude of each IMF.

We applied EEMD to 30 min time series with 10 Hz resolution after removing the 30 min block average, so the overall residual here is different from the original definition in *Huang et al.* [1998]. Thirteen IMFs were extracted with one residual, marked as the fourteenth IMF (IMF_{14}). The flux contribution from particular IMFs (IMF_k) can be calculated using the following equation:

$$\overline{w'c'}_k = \frac{1}{2}\left(\sum_{i=1}^{14} \overline{\mathrm{IMF}_{i,\,w}\cdot\mathrm{IMF}_{k,c}} + \sum_{j=1}^{14} \overline{\mathrm{IMF}_{k,w}\cdot\mathrm{IMF}_{j,c}}\right), \qquad (3)$$

where c represents u, θ, or q and $k = 1, 2, \ldots, 14$. The total covariance calculated from all IMFs is equivalent to the covariance calculated using the traditional eddy covariance method [*Barnhart et al.*, 2012].

4. Results and Discussion

4.1. Flux Convergence/Divergence and Evidence of Large Eddies

Figure 3 shows typical daytime variations in energy fluxes (R_n, LE, and sensible heat flux H), $\overline{u'w'}$, ζ, γ_{uw}, and $\gamma_{\theta q}$ for 8.7 m and 2.7 m at our site over the flat cotton field on 7 August 2000. Due to the lack of clouds, R_n follows a nearly ideal cosine shape with a maximum value about 700 W m^{-2} at 13:00 PDT (local noon). LE and $\overline{u'w'}$ at both heights exhibit large point-to-point variations during the daytime (Figures 3a and 3c), whereas H at 8.7 m and 2.7 m has small positive values in the morning and becomes negative in the afternoon in Figure 3b. FC and FD in LE occurred occasionally between 2.7 and 8.7 m. What processes caused flux convergence and divergence in LE? Previous studies using the EBEX data set indicated that large eddies played significant roles in affecting turbulence structures and flux transport [e.g., *Zhang et al.*, 2010]. It remains unclear whether these large eddies also modulated turbulence structures and flux transport differently for different heights, leading to the observed FC and FD. It has not been extensively studied about whether and how these large eddies affect different turbulence quantities in different ways that lead to FC and FD.

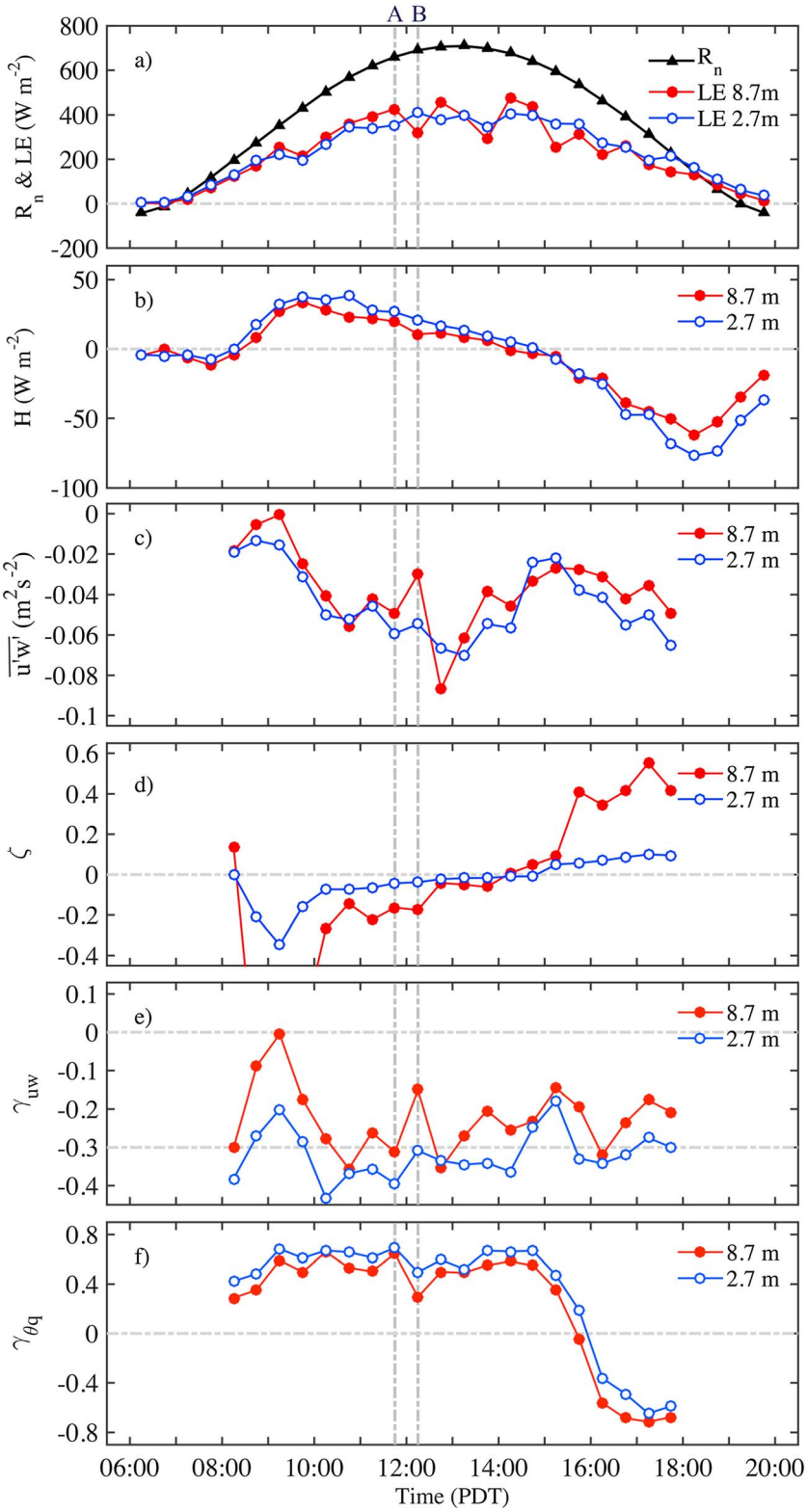

Figure 3. Daytime variations of (a) net radiation (R_n) and latent heat flux (LE), (b) sensible heat flux (H), (c) $\overline{u'w'}$, (d) stability parameter, $\zeta = (z - d)/L$, (e) correlation coefficient of u and w, and (f) correlation coefficient of θ and q at 2.7 and 8.7 m on 7 August 2000. The local noon was about 13:00 PDT. A (11:30–12:00 PDT) and B (12:00–12:30 PDT) are periods for specific investigations, see Figure 4.

In the morning, the ASL was typically unstable followed by a transition in the late morning or early afternoon to near-neutral or stable conditions (the stable ASL beneath the CBL) (Figure 3d). The existence of negative H and the development of a stable ASL reveal the influence of an "oasis effect" and horizontal advection [*Oncley et al*., 2007] under warm (dry)-to-cool (wet) transition from the upstream drier patches to the wet cotton field [*Kaimal and Finnigan*, 1994; *Zhang et al*., 2010]. This horizontal advection is believed to be partially responsible for the late afternoon surface energy imbalance and vertical flux divergence [*Oncley et al*., 2007]. However, the flux convergence and divergence between 2.7 m and 8.7 m, especially in the morning under unstable conditions, cannot be fully explained by the influence of horizontal advection due to the soil moisture heterogeneity [*Oncley et al*., 2007; *Zhang et al*., 2010].

Högström [1990] showed that γ_{uw} can be used to examine the disturbance of "inactive" turbulence (i.e., large eddies) in the ASL, and lower correlation coefficients (less negative values of γ_{uw}) suggest more large eddies contained in the ASL because they increase σ_u and σ_w but do not contribute to $\overline{u'w'}$. A mean value of γ_{uw} for near-neutral ASL is -0.3 [*Högström*, 1990]. In the present study, γ_{uw} exhibited large point-to-point variations with a magnitude often larger than -0.3 at 8.7 m. It is interesting to note that under slightly unstable to near-neutral conditions around noon the γ_{uw} variations at 8.7 m correspond to the variations in LE, with low-correlation coefficients for u and w corresponding to low turbulent transport of water vapor (Figures 3a and 3e). For example, from 11:30–12:00 to 12:00–12:30 PDT, LE at 8.7 m dropped about 100 W m^{-2} while the magnitude of γ_{uw} decreased about 0.2. The γ_{uw} variations at 2.7 m showed similar trends but with more negative values than 8.7 m. $\gamma_{\theta q}$ can also be used as a criteria to evaluate the effects of large eddies since large eddies originating from nonlocal regions can change the scalar-scalar source and sink distributions in the ASL [*McNaughton and Laubach*, 1998; *Ruppert et al*., 2006; *Katul et al*., 2008; *Huang et al*., 2009]. As shown in Figure 3f, $\gamma_{\theta q}$ at 8.7 m was consistently smaller than at 2.7 m during unstable conditions in the morning and early afternoon, suggesting greater dissimilarities in θ-q covariance at 8.7 m than 2.7 m. In summary, the diurnal variations of turbulent fluxes, γ_{uw} and $\gamma_{\theta q}$ at 8.7 m and 2.7 m demonstrate that large eddies have greater influences on turbulence at 8.7 m than at 2.7 m, consistent with *Zhang et al*. [2010].

The time series turbulence data also provide evidence of large eddies with large-scale coherent motions observed in u', w', θ', and q' at 8.7 m and 2.7 m (Figure 4). In order to make the figure more readable, the data were reduced from 10 to 1 Hz resolution by applying block average. To highlight ramp-like patterns, the traces in Figure 4 represent the sum of IMF_{7-12} by using EEMD in section 3.2 to remove turbulent signals of IMF_{1-6}. Twelve IMFs were extracted from the reduced data, and IMF_{7-12} represents eddies with time scales larger than about 50 s. Note that the time series data with those modes keep most of the ramp-like patterns, indicating the effectiveness of EEMD in decomposing turbulence data. Figure 4 (right and left columns) exhibits the half-hour time series for 11:30–12:00 PDT (i.e., a FC case; A in Figure 3a) and 12:00–12:30 PDT (i.e., a FD case; B in Figure 3a), respectively. The stability parameter is comparable for point A and B as shown in Figure 3d. For both FC and FD, distinct ramp structures occur occasionally and coherently at 8.7 m and 2.7 m in the θ' and q' time series (e.g., 600–900 s in Figure 4 (left column) and 900–1500 s in Figure 4 (right column)), but with no well-defined time lags, and these structures also correspond to the ramp patterns in u' and w' time series. As reflected by the ramp intensity, these temperature and water vapor ramp structures are less intense at 8.7 m ($I_\theta = 0.31$ (0.33) and $I_q = 1.62$ (1.73) for FC (FD)) than at 2.7 m ($I_\theta = 0.46$ (0.48) and $I_q = 2.02$ (2.67) for FC (FD)), whereas the corresponding ramp intensity in the w' time series is stronger at 8.7 m ($I_w = 0.33$ (0.43)) than 2.7 m ($I_w = 0.28$ (0.38) for FC (FD)). The ramp intensity is defined as the sum of the amplitude of ejections (updrafts) and sweeps (downdrafts) in the 30 min time series of different quantities [*Zhang et al*., 2011]. The reader is referred to *Zhang et al*. [2011] for a complete detail on the calculation of ramp intensity. These bursts lead to positive bursts of $w'q'$ and $w'\theta'$ and negative bursts of $u'w'$ at 8.7 m and 2.7 m for both FC and FD. Clearly, large eddies have a large impact on turbulence structures and vertical transport of momentum, temperature, and water vapor. As reflected by the burst intensity for $w'q'$, these ramp structures contribute more to $w'q'$ at 8.7 m than 2.7 m for FC (e.g., 600–900 s in Figure 4 (left column)). Our results likely suggest that, despite the smaller q' ramp intensity at 8.7 m, the greater w' ramp intensity at 8.7 m is primarily responsible for the greater contribution of the bursts to $w'q'$. We conducted sensitivity tests to quantify changes in $w'q'$ by reducing the ramp intensity for w' at 8.7 m. Our test results indeed indicate that reducing the w' ramp intensity at 8.7 m without changes in the q' ramp intensity at the both heights decreases the contribution of the bursts to $w'q'$ and thus a decrease in LE at 8.7 m. For example, when

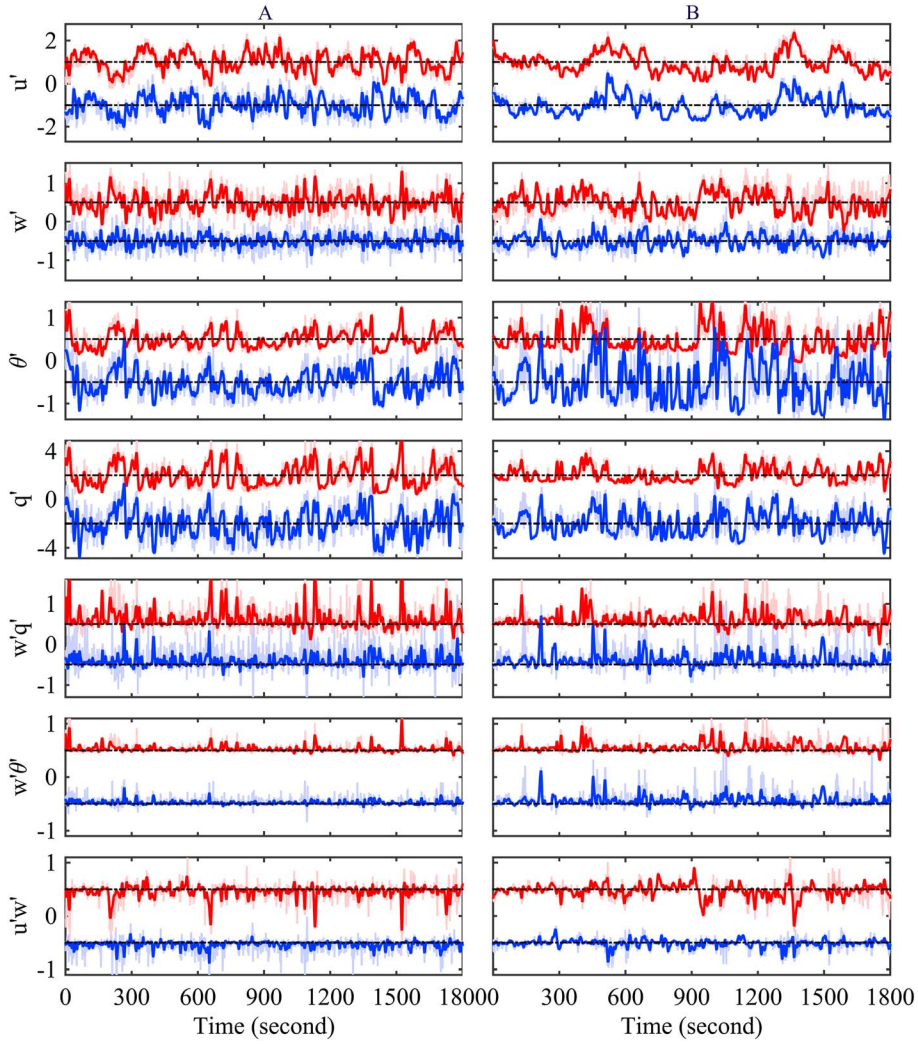

Figure 4. The 30 min time series of u', w', θ', and q', and their contribution to fluxes of w-q, w-θ, and u-w for the (a) FC case and (b) FD case, A and B in Figure 3, respectively, at 8.7 m (red lines) and 2.7 m (blue lines). The shading denotes the time series with 1 Hz resolution, and the traces represent the sum of IMF_{7-12}. Note that the fluctuations at 8.7 m and 2.7 m were shifted upward and downward to make the plot more readable (i.e., ±1 for u', ±2 for q', and ±0.5 for the rest).

reducing the w' ramp intensity at 8.7 m to about 50% of its original value, LE at 8.7 m decreased by about 40%. In addition, when replacing the w′ time series at 8.7 m to that at 2.7 m, LE at 8.7 m decreased by about 70%, while replacing the q' time series at 8.7 m to that at 2.7 m, LE at 8.7 m only changed by about 20%. For FD, however, large eddies depress the ramp intensities for temperature and specific humidity at 8.7 m but not at 2.7 m (e.g., 500–900 s in Figure 4, right column), leading to a smaller LE at 8.7 m than at 2.7 m. In the mornings with unstable conditions, air temperature and specific humidity decreased with height, and wind speeds increased with height in the ASL. It is expected that large eddies, if originating outside the ASL and impinging to the surface, are dry and cool, causing relatively smaller ramp intensities for temperature and specific humidity at high levels than at low levels. When large eddies are generated near the surface and move upward, however, they are wet and warm, causing relatively smaller ramp intensities for temperature and specific humidity at low levels than at high levels. The weaker ramp structures at 8.7 m than 2.7 m suggest that the large eddies in this study originated aloft outside the ASL.

4.2. Temporal and Spatial Scales of Large Eddies and Their Influences on Flux Convergence/Divergence

To illustrate temporal and spatial scales of the large eddies and potential differences in these characteristics between the two heights and between FC and FD, the continuous wavelet transform was applied to the

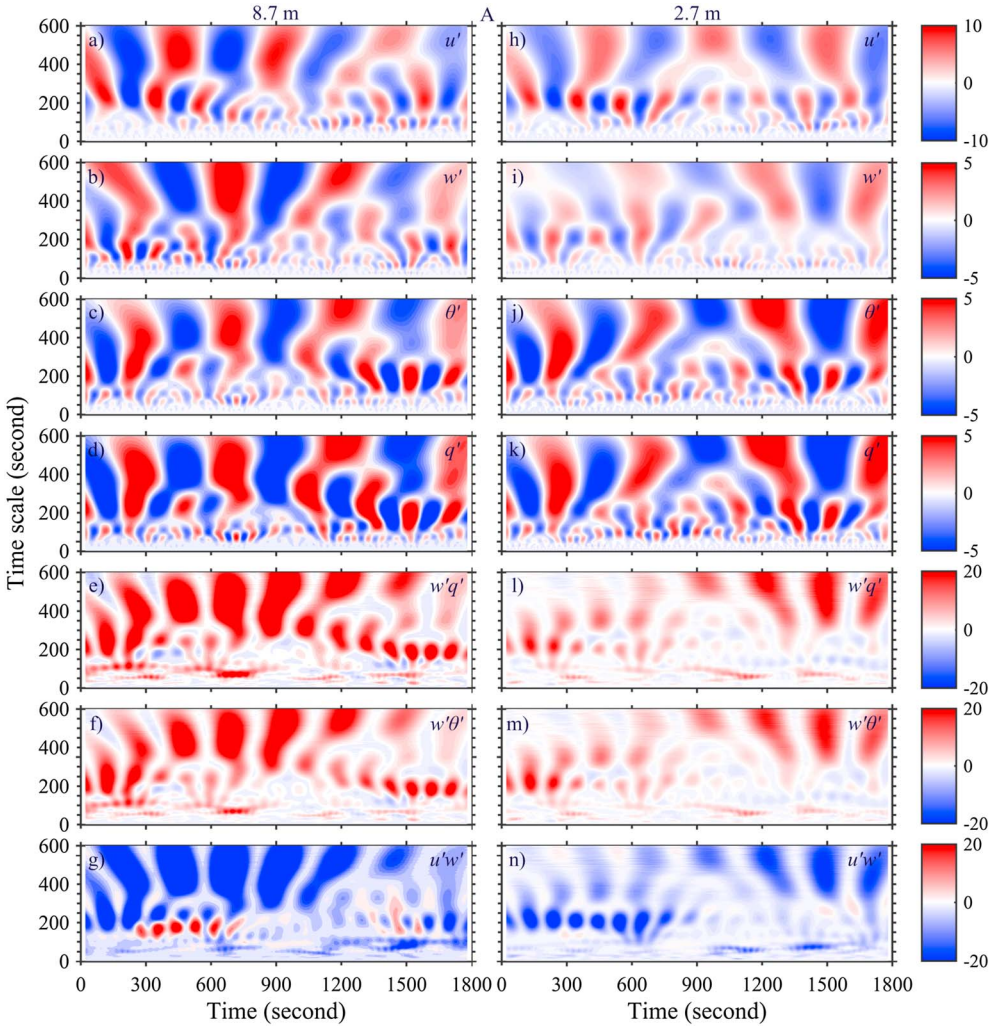

Figure 5. The time and scale distribution of the wavelet transforms of the 30 min time series of (a and h) u', (b and i) w', (c and j) θ', and (d and k) q' fluctuations and the wavelet local cospectra of (e and l) w-q, (f and m) w-θ, and (g and n) u-w for the FC case (A in Figure 3) at 8.7 m (Figures 5a–5g) and 2.7 (Figures 5h–5n), respectively.

30 min time series of u', w', θ', and q' for FC and FD at 8.7 m and 2.7 m. Figures 5 and 6 display the time and scale distributions of their wavelet transforms at 8.7 m (a–g) and 2.7 m (h–n) for FC and FD, respectively. The disorganized field near the bottom of each plot (i.e., Figures 5a–5d, 5h–5k, 6a–6d, and 6h–6k) is contributed primarily by background turbulence with time scales of less than about 10 s, consistent with *Gao and Li* [1993]. As the time scale increases, the distributions tend to be organized into discrete plume-like structures near the time scale of 50 s. At the top of each plot, the large positive (red color) and negative (blue color) centers correspond to the low-frequency trends appearing in the corresponding time series as shown in Figure 4. It should be stressed that these low-frequency trends have a time scale on the order of minutes (~500 s) and could be associated with large eddies or thermal plumes with a spatial scale of about 1000 m. In the middle of each plot (50 s $<$ time scale $<$ 500 s), it seems that the plume-like patterns gradually merge into some larger structures, while the atmospheric boundary layer (ABL) large eddies continuously break down into smaller structures. Therefore, the middle part of each plot is more likely a region where ABL circulations interact with organized structures [*McNaughton and Laubach*, 2000; *Högström et al*., 2002; *McNaughton and Brunet*, 2002]. The strength and continuity of the interactions are associated with the turbulent exchange of momentum, temperature, and water vapor. However, in the absence of a three-dimensional visualization, we can only postulate about the ways of interaction between large-scale motions and locally generated turbulence in the ASL.

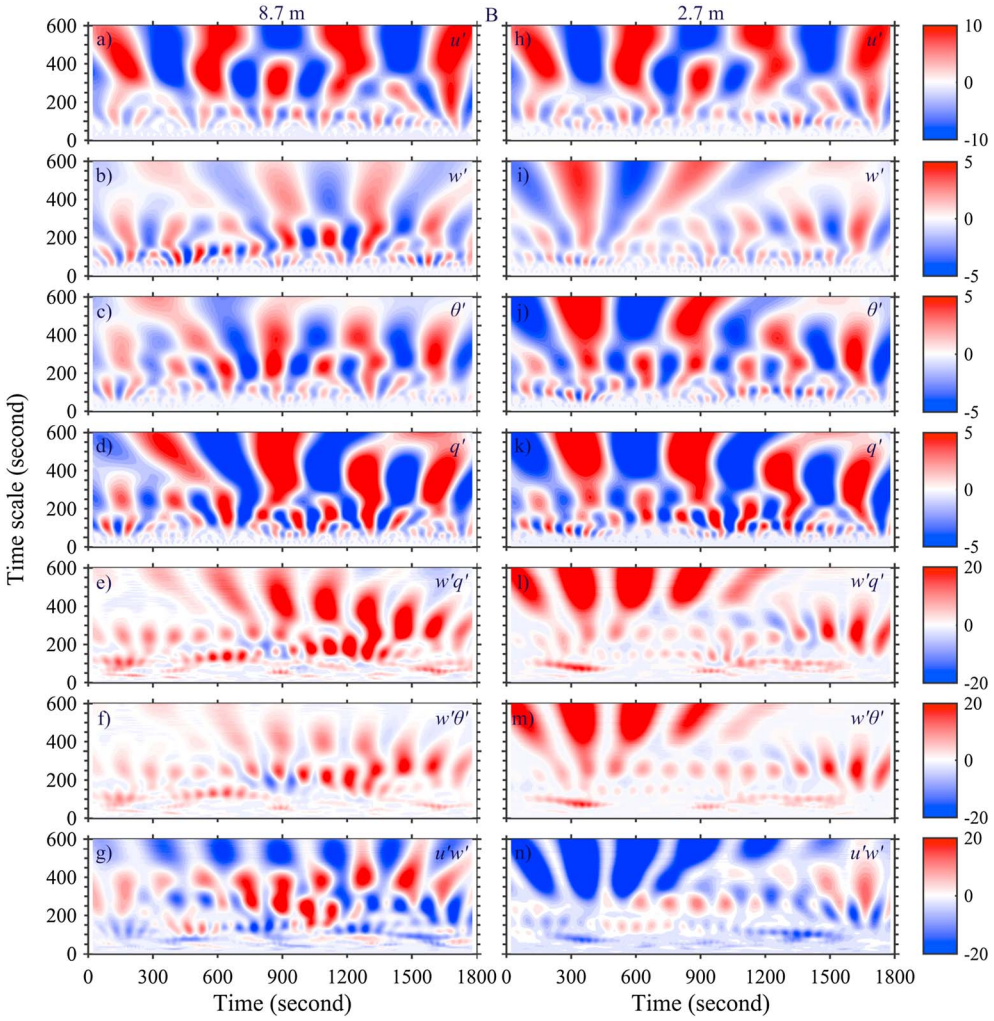

Figure 6. The time and scale distribution of the wavelet transforms of the 30 min time series of (a and h) *u*, (b and i) *w*, (c and j) θ, and (d and k) *q* fluctuations and the wavelet local cospectra of (e and l) *w*-*q*, (f and m) *w*-θ, and (g and n) *u*-*w* for the FD case (B in Figure 3) at 8.7 m (Figures 6a–6g) and 2.7 (Figures 6h–6n), respectively.

For each case, the distributions of transformed temperature and water vapor at each height (8.7 m and 2.7 m) have similar patterns, with the warm and cool centers (red and blue centers in Figures 5c, 5j, 6c, and 6j) related to the moist and dry centers (red and blue centers in Figures 5d, 5k, 6d, and 6k) with the time scales of 50–500 s (i.e., approximately a few hundred meters in spatial scales). These warm-moist and cool-dry centers also correspond to the organized updrafts and downdrafts, respectively, as identified in Figures 5b, 5i, 6b, and 6i, as seen from the time series data in Figure 4. The transformed vertical velocity at 8.7 m for both FC and FD has a distribution much different from that at 2.7 m in terms of the locations and the magnitudes of the organized structures. The differences in the magnitudes of the organized structure between 8.7 m and 2.7 m for FC are more prominent than those for FD, particularly for the *w* local wavelet distribution. For FC, the organized structures at 8.7 m have much greater magnitudes than at 2.7 m though the locations of these structures are similar between 8.7 m and 2.7 m; for FD, there is substantial difference in the distributions of the organized structures between 8.7 m and 2.7 m. It appears that changes in the organized structures in θ' and q' at 8.7 m and 2.7 m for both FC and FD correspond to those in w'. Therefore, the distributions of the local wavelet cospectra for *w*-*q*, *w*-θ, and *u*-*w* at 8.7 m (Figures 5e–5g and 6e–6g) have patterns dissimilar to those at 2.7 m (Figures 5l–5n and 6l–6n). For FC, the organized structures illustrated in the local wavelet distributions of *w*-*q*, *w*-θ, and *u*-*w* at 8.7 m are stronger than 2.7 m. Note that the difference in patterns of the organized structures between 8.7 m and 2.7 m is more significant in FD than those in FC. Positive flux contribution is present in the local wavelet cospectra of *w*-*q* and *w*-θ and negative flux contribution in *u*-*w* at 8.7 m and

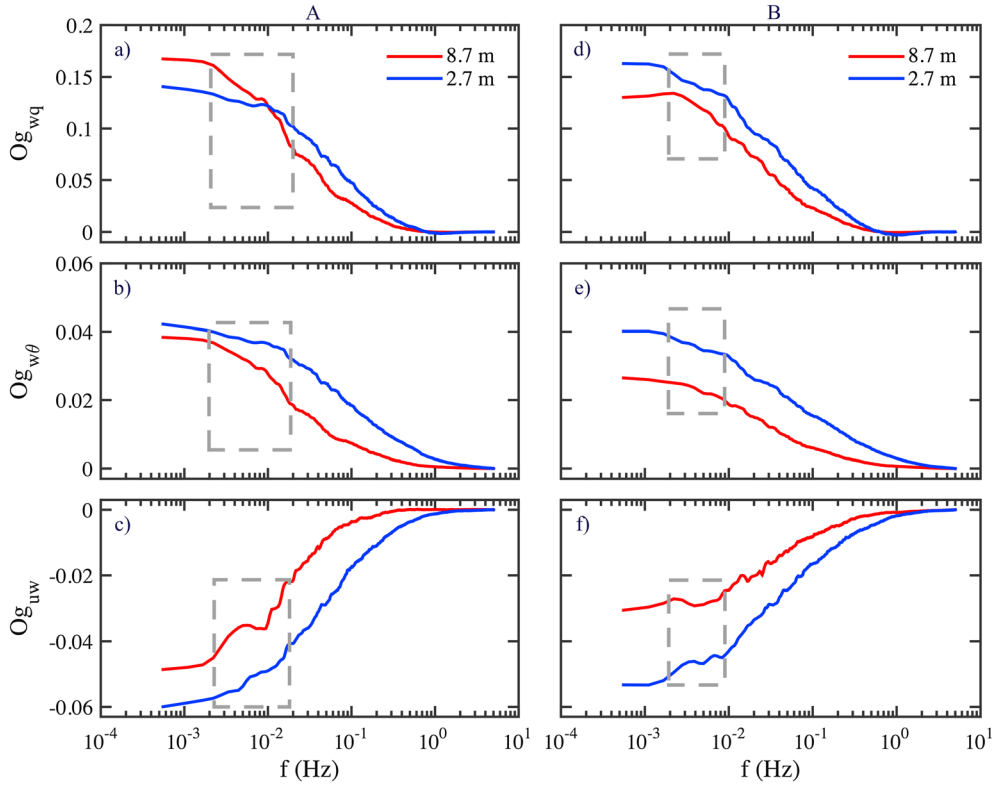

Figure 7. The Ogive function of (a and d) *w-q*, (b and e) *w-θ*, and (c and f) *u-w* for the FC case (Figures 7a–7c) and FD case (Figures 7d–7f). The gray box denotes the frequency range over which the *w-q* Ogive function increases more rapidly at 8.7 m than at 2.7 m.

2.7 m (Figures 5g and 6g). Note that larger magnitudes of these structures in the plots of local wavelet cospectra do not necessarily correspond to higher flux contributions. The magnitudes denote the strength of the corresponding structures: the larger the magnitudes, the greater the fluctuations of the corresponding quantities at a given scale. Our results indicate that for FC, large eddies enhance the fluctuations in turbulence and scalar quantities and flux transport more significantly at 8.7 m than 2.7 m, leading to the LE flux convergence; for FD, however, large eddies depress the fluctuations at 8.7 m, but do not impact on those at 2.7 m, leading to the LE flux divergence.

The Ogive function was proposed to investigate flux contribution of eddies with different scales [e.g., *Oncley et al*., 1996; *Charuchittipan et al*., 2014]. We performed the Ogive test to the two 30 min time series in FC and FD to examine large eddies in a more quantitative way than the wavelet transform analysis above. Apparently, the low-frequency motions with their natural frequency $f < 0.002$ Hz (i.e., approximately > 1000 m in spatial scales) have no significant contribution to the fluxes, and the difference of the fluxes between 8.7 m and 2.7 m is predominantly caused by the eddies with their frequencies larger than 0.002 Hz (Figure 7). For both FC and FD, in the high-frequency ranges ($f > 0.07$ Hz), the Ogive function at 2.7 m is higher in magnitude for *w-q* and *w-θ* and lower for *u-w* than at 8.7 m, demonstrating that eddies with $f > 0.07$ Hz (i.e., a few tens of meters in spatial scales) have more flux contribution at 2.7 m than at 8.7 m. In addition, the slopes of the Ogive function for *w-q* and *w-θ* at 8.7 m and 2.7 m are similar over 0.02 Hz $< f <$ 0.07 Hz, suggesting the same flux contribution of *w-q* and *w-θ* at both heights from this frequency range. For FC, the Ogive function for *w-q* and *w-θ* at 8.7 m increases more rapidly than at 2.7 m over 0.002 Hz $< f <$ 0.02 Hz (i.e., 50 s < time scales < 500 s; the gray box in Figure 7), indicating that large eddies with sizes of several hundred meters contribute more to $\overline{w'\theta'}$ and $\overline{w'q'}$ at 8.7 m than at 2.7 m (Figures 7a and 7b). However, these large eddies contribute less to $\overline{u'w'}$ mainly due to the positive flux contribution from part of these eddies as shown in Figure 5g. For FD, the slope of the Ogive function for *w-q* at 8.7 m is still larger than that at 2.7 m over 0.002 Hz $< f <$ 0.02 Hz but much less than that for FC, suggesting that for FD large eddies with sizes of several

hundred meters at 8.7 m are depressed compared to FC (Figure 7d). In addition, the Ogive functions for $\overline{w'\theta'}$ and $\overline{u'w'}$ at 2.7 m are still higher than those at 8.7 m (Figures 7e and 7f). Our results suggest that large eddies with the sizes of several hundred meters (0.002 Hz $< f <$ 0.02 Hz) are primarily responsible for the observed FC and FD through modulating their contributions to fluxes in different ways at the two levels.

4.3. Statistical Analysis of Influence of Large Eddies on Turbulent Transport

4.3.1. Influence of Large Eddies on Turbulence Statistics

To examine whether the characteristics identified in the case study above from individual data points are applicable to other data points, the data set under unstable conditions was separated into two groups (FC and FD) based on the description in section 2.2. Table 1 summarizes the fluxes and turbulence statistics for FC (34 runs) and FD (13 runs) under unstable conditions. For the FC group, LE at 8.7 m is 21% larger than at 2.7 m; whereas H at 8.7 m is 11% smaller than at 2.7 m. For the FD group, LE and H at 8.7 m are 18% and 45% smaller than at 2.7 m, respectively. Since MOST requires vertical flux divergence of less than 10% in the ASL, the FC and FD magnitudes for those runs are thus substantially larger than the ranges predicted by the MOST theory and significantly exceed the estimated measurement errors of eddy covariance system [*Mauder et al*., 2007; *Oncley et al*., 2007]. For both groups, the magnitudes of σ_u/u_* and σ_v/u_* are comparable, and they increase slightly from 2.7 m to 8.7 m. These values are consistent with those reported in the literature in the near-neutral ASL (e.g., 2.4–2.8 in *Högström* [1990]). The σ_w/u_* increases by 20% from 2.7 m to 8.7 m for the FC group under unstable conditions with a significance level of 95%. Also, the difference in σ_w/u_* between these two levels is larger than that reported in *Högström* [1990] under near-neutral conditions (i.e., 8% between 3 m and 6 m). However, for the FD group, the increase of σ_w/u_* with height is not as significant as the FC group, which could be caused by the difference of atmospheric stratifications. The atmospheric surface layer was more unstable for FC group than for the FD group. As illustrated in *Zhang et al*. [2011], the w ramp intensity decreases as the ASL changes from unstable to near-neutral conditions. γ_{uw} and $\gamma_{\theta q}$ at 8.7 m are slightly smaller than at 2.7 m for both groups, suggesting more significant effects of large eddies on turbulence structures at 8.7 m than at 2.7 m. It is worth noting that at 8.7 m, σ_w/u_*, γ_{uw}, and $\gamma_{\theta q}$ for the FC group are significantly larger than those for the FD group (a significance level of 95%), indicating the stronger effects of large eddies on turbulence structures. To characterize the properties of large eddies and their influence on the turbulent transport, u, v, w, q, and θ spectra and cospectra of w-q, w-θ, and u-w will be examined in the next two subsections.

4.3.2. Influence of Large Eddies on Turbulence Spectra

Figure 8 shows the averaged normalized power spectra of u, v, w, q, and θ as a function of the nondimensional frequency, $n = f(z-d)/u$ (where f is the natural frequency and z is the measurement height), at 8.7 m and 2.7 m for the FC group and the FD group. The individual spectra were scaled before averaging, using the value of the relevant scaling parameter at 2.7 m. The shaded areas represent the standard deviations of the averaged spectra. For comparison, we also added the Kansas spectra under near-neutral conditions (black dash-dotted lines) [*Kaimal et al*., 1972]. For both groups (FC and FD), the u, v, and w spectra in the inertial subrange ($n > 0.4$) at 8.7 m and 2.7 m have comparable magnitudes, and both are close to the corresponding Kansas spectra. However, the u, v, and w spectra over the middle- to low-frequency ranges ($n < 0.07$) largely deviate from the Kansas spectra. Broadening and enhanced variability of these spectra over the middle- to low-frequency ranges indicate the disturbance of large eddies in the ASL [*McNaughton and Laubach*, 2000; *Zhang et al*., 2010]. The scalar spectra are consistently lower in magnitudes at 8.7 m than at 2.7 m over the whole frequency range, which is largely attributed to the decreased vertical gradients of water vapor and temperature with heights in the unstable ASL. The large standard deviations in all these spectra in the middle- to low-frequency ranges suggest the large variability in the influence of large eddies.

In the middle- to low-frequency ranges, the spectral peaks are considered to be associated with the dominant sizes of large eddies [*McNaughton and Laubach*, 2000; *Högström et al*., 2002; *Zhang et al*., 2010]. For the FC group, the u spectra have one dominant peak appearing in the middle- to low-frequency ranges at both heights of 8.7 m and 2.7 m (i.e., red and blue arrows in Figure 8a, respectively), with the same natural frequency ($f = 0.008$ Hz), whereas the u spectra at 8.7 m have more energy than at 2.7 m over the middle- to low-frequency ranges (i.e., $n < 0.07$). For the FD group, however, the u spectrum only at 8.7 m shows a peak with a natural frequency of 0.005 Hz (i.e., red arrow in Figure 8f), indicating that the dominant size of large eddies (~400 m) for the FD group is relatively larger than for the FC group (~250 m). The scales of these

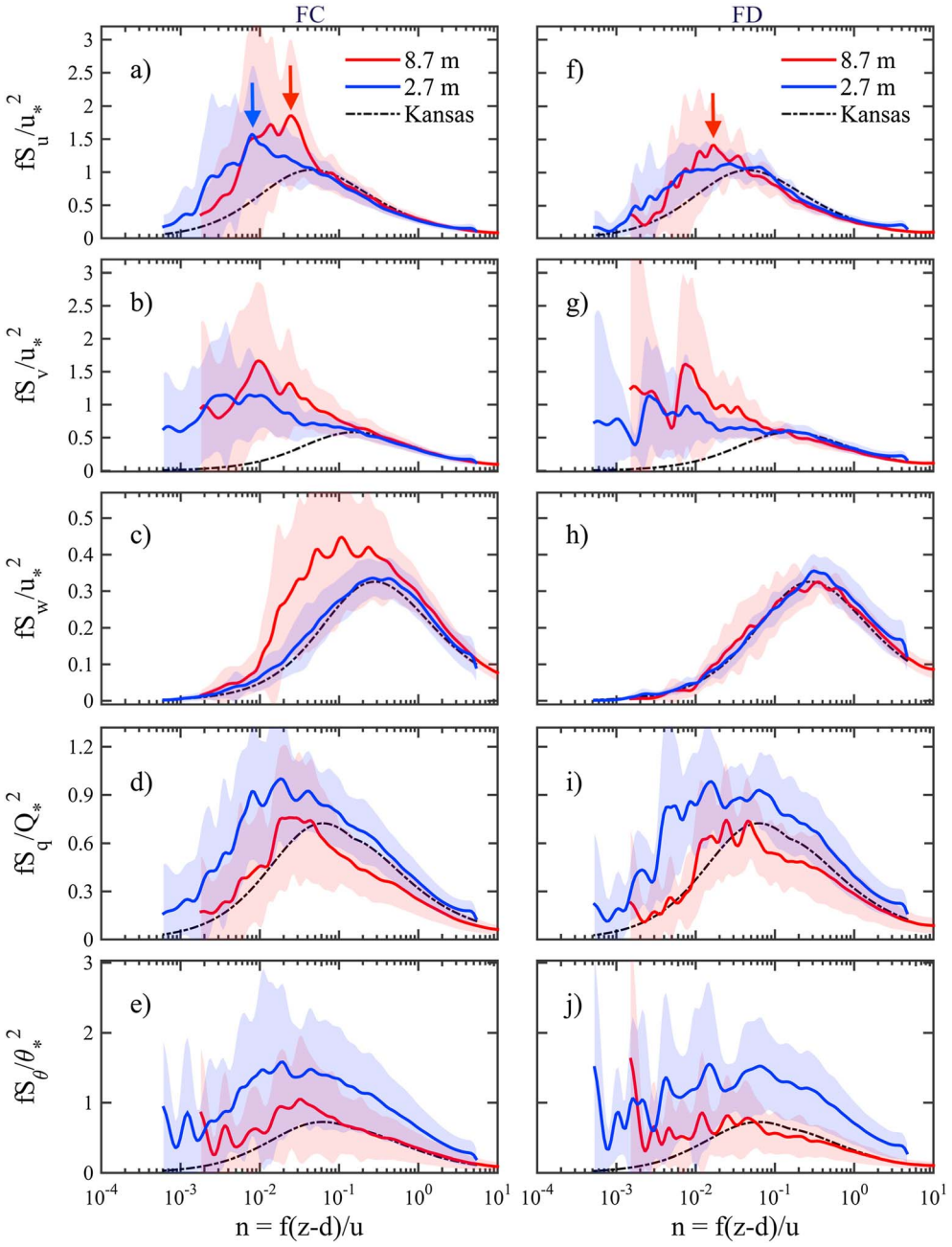

Figure 8. Normalized global wavelet spectra of (a and f) u, (b and g) v, (c and h) w, (d and i) q, and (e and j) θ as a function of the normalized frequency $n = f(z - d)/u$ at 8.7 and 2.7 m under flux convergence (FC: 34 runs, Figures 8a–8e) and flux divergence (FD: 13 runs, Figures 8f–8j) under unstable conditions. All power spectra are normalized by the value of the scaling parameter at 2.7 m. The shaded area represents the standard deviation of the averaged spectra. The black lines are the corresponding Kansas spectra under near-neutral conditions [*Kaimal et al.*, 1972].

dominant large eddies obtained from these averaged spectra are consistent with the case study in sections 4.1 and 4.2. For both FC and FD group, the v spectra at 8.7 m are also enhanced more by large eddies than at 2.7 m in the middle- to low-frequency ranges. It is interesting to note that for the FC group, the w spectrum at 8.7 m shows significant enhancement in $0.01 < n < 0.4$, but no enhancement for the FD group in these frequencies (Figures 8c and 8h), corresponding to more depression of the u and v spectra over the middle- to low-frequency ranges for the FD group than the FC group (Figures 9a and 9b). Over the range of $0.01 < n < 0.4$, the u and v spectra at 8.7 m contain about 12% and 8% more energy for FC group than FD

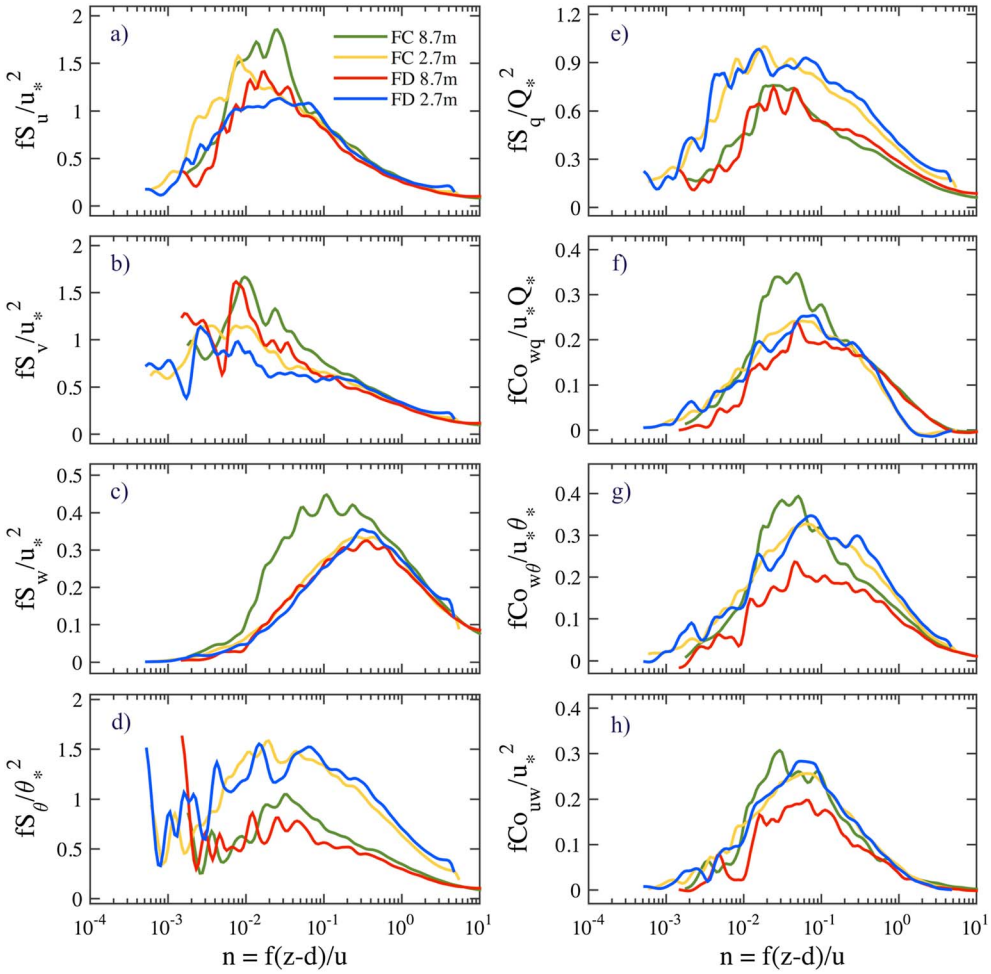

Figure 9. Merged normalized global wavelet spectra of (a) *u*, (b) *v*, (c) *w*, (d) *q*, and (e) θ and cospectra of (f) *w*-*q*, (g) *w*-θ, and (h) *u*-*w* under flux convergence (FC) and flux divergence (FD) conditions in Figures 8 and Figure 10.

group, respectively. The enhancement of *w* spectrum at low-frequency ranges has been observed previously in the disturbed ASL [e.g., *Högström et al*., 2002; *Zhang et al*., 2010]. It appears likely that these vertical motions are associated with coherent downdrafts and updrafts [*McNaughton and Laubach*, 2000], which are initiated by inactive large eddies near the ground occurring as streak patterns of horizontal velocity [*McNaughton and Brunet*, 2002]. The scalar spectra (*q* and θ) at both heights also show similar peaks in the middle- to low-frequency ranges for the FC (Figures 8d and 8e) and FD groups (Figures 8i and 8j), indicating that large eddies which distort the flow fields also affect the scalar distributions, in consistent with the case study in section 4.2.

Note that a spectral gap is not present in the middle- to low-frequency ranges of the wind velocity spectra as argued in the literatures [e.g., *McNaughton and Laubach*, 2000]. The fall-off power laws of the spectra in the middle- to low-frequency ranges may indicate the ways of interaction between the large eddies and locally generated turbulence in the ASL [*McNaughton and Laubach*, 2000; *Högström et al*., 2002; *Zhang et al*., 2010]. Table 2 lists the fall-off power laws of the spectra in the middle- to low-frequency range. For the FC group, the *u* spectrum at 2.7 m falls off as a -1.2 power law over the range of $0.007 < n < 0.07$, whereas the *u* spectrum at 8.7 m falls off from the peak toward higher frequencies with nearly a $-5/3$ power law in the range $0.03 < n < 0.07$. For the FD group, the *u* spectra at 8.7 m and 2.7 m fall off as a -1.2 and -1.0 power law over the range of $0.03 < n < 0.07$, respectively. The *w* spectra at 8.7 m and 2.7 m follow a -1.0 power law for $0.07 < n < 0.3$ for both FC and FD groups, whereas the -1.0 power law appears within $0.03 < n < 0.07$ only for the FC group at 8.7 m. In addition, the scalar spectra at 8.7 m and 2.7 m follow similar power laws in the middle- to low-frequency ranges for both FD and FC groups. These results suggest that the ways of

Table 2. Summary of the Fall-Off Power Laws of the Spectra in the Middle- to Low-Frequency Range for Flux Convergence (FC) and Flux Divergence (FD)

		$0.007 < n < 0.03$		$0.03 < n < 0.07$		$0.07 < n < 0.3$	
		FC	FD	FC	FD	FC	FD
u	8.7 m	−0.8	−0.5	−5/3	−1.2	−1.4	−1.2
	2.7 m	−1.2	−0.8	−1.2	−1.0	−1.4	−5/3
v	8.7 m	−1.3	−1.4	−1.3	−5/3	−1.3	−1.0
	2.7 m	−1.3	−1.0	−1.1	−1.0	−1.2	−1.0
w	8.7 m	0.1	0.0	−1.0	−0.4	−1.0	−1.0
	2.7 m	−0.2	−0.2	−0.4	−0.4	−1.0	−1.0
q	8.7 m	−0.3	−0.1	−1.0	−1.0	−1.2	−1.2
	2.7 m	−0.8	−0.8	−1.0	−1.0	−1.4	−1.4
θ	8.7 m	−0.6	−1.0	−1.0	−1.0	−1.4	−1.2
	2.7 m	−1.0	−1.0	−1.2	−1.2	−1.4	−1.4

interaction between the large eddies and locally generated turbulence at 8.7 m and 2.7 m are different for the FC and FD groups.

In summary, comparison of the u spectra at 8.7 m between the FC group and the FD group (Figure 9a) shows that the peak frequency for the FC group ($f = 0.008$ Hz) shifts to higher frequencies compared to the FD group ($f = 0.005$ Hz), indicating that the averaged size corresponding to dominant large eddies for the FC group (~250 m) is relatively smaller than for the FD group (~400 m). On the other hand, the w spectrum at 8.7 m contains more energy for the FC group than the FD group, especially between $0.01 < n < 0.5$ (Figure 9c). Our results confirm that large eddies with relatively smaller averaged sizes are more vertically active than large eddies with relatively larger averaged sizes in influencing turbulence in the ASL [*McNaughton and Laubach*, 2000; *Zhang et al*., 2010]. The enhancement of the w spectra in the middle- to low-frequencies is associated with the ways of interaction between large eddies and ASL turbulence.

4.3.3. Influence of Large Eddies on Turbulence Cospectra and Flux Convergence/Divergence

Figure 10 shows the normalized cospectra of w-q, w-θ, and u-w as a function of n. The cospectra were normalized by the relevant scaling parameter at 2.7 m. For the FC group, there is an obvious convergence in the w-q cospectra at 8.7 and 2.7 m (i.e., higher w-q cospectra at 8.7 m than at 2.7 m) over frequency range of $0.01 < n < 0.1$, reflecting the different influences of the large eddies with the size of several hundred meters on turbulent exchanges between 8.7 m and 2.7 m (Figure 10a), which is consistent with the case study in section 4.2. Apparently, this cospectral convergence over this frequency range is mainly responsible for the observed LE convergence. The flux convergence in LE is primarily caused by the enhancement of w spectra in the middle- to low-frequency ranges, in consistent with the results obtained in the case study above. The frequency range ($0.01 < n < 0.4$) corresponding to the flux convergence of LE is largely associated with the w spectra enhancement over the range of $0.01 < n < 0.1$. Note that the cospectral convergence over the range of $n > 0.4$ is caused by the horizontal sensor displacement between CSAT3 and KH20 [*Oncley et al*., 2007; *Horst and Lenschow*, 2009]. Our calculations indicate that this high-frequency loss accounts for only about 6% difference of water vapor flux between 8.7 m and 2.7 m. The w-θ and u-w cospectra show some convergence over a narrow frequency range ($0.01 < n < 0.04$), suggesting that these large eddies are also active in transporting sensible heat and momentum fluxes (Figures 10b and 10c). However, the increased convergence in the w-θ and u-w cospectra over $0.01 < n < 0.04$ is smaller than the decreased divergence in the w-θ and u-w cospectra over the rest of the frequency ranges, leading to the overall smaller fluxes of sensible heat and momentum at 8.7 m than those at 2.7 m.

For the FD group, the w-q, w-θ, and u-w cospectra show consistent convergence over the entire frequency range (Figures 10d–10f). Again, about 6% of the w-q flux convergence for $n > 0.5$ is caused by high-frequency loss due to the separation of CSAT3 and KH20. The w-θ and u-w cospectra illustrated consistent divergence between 8.7 and 2.7 m (Figures 10e and 10f). We attribute the divergence of the w-q, w-θ, and u-w cospectra to the depression or reduction of the large eddies with the size of several hundred meters (i.e., $0.002\ \text{Hz} < f < 0.02\ \text{Hz}$) that are active in the FC group. These large eddies depress the flow and scalar field and thus turbulent transport at 8.7 m but not at 2.7 m, which supports the conclusion from the case study. Our analysis suggests that the flux convergence of LE between 8.7 m and 2.7 m was mainly caused by the

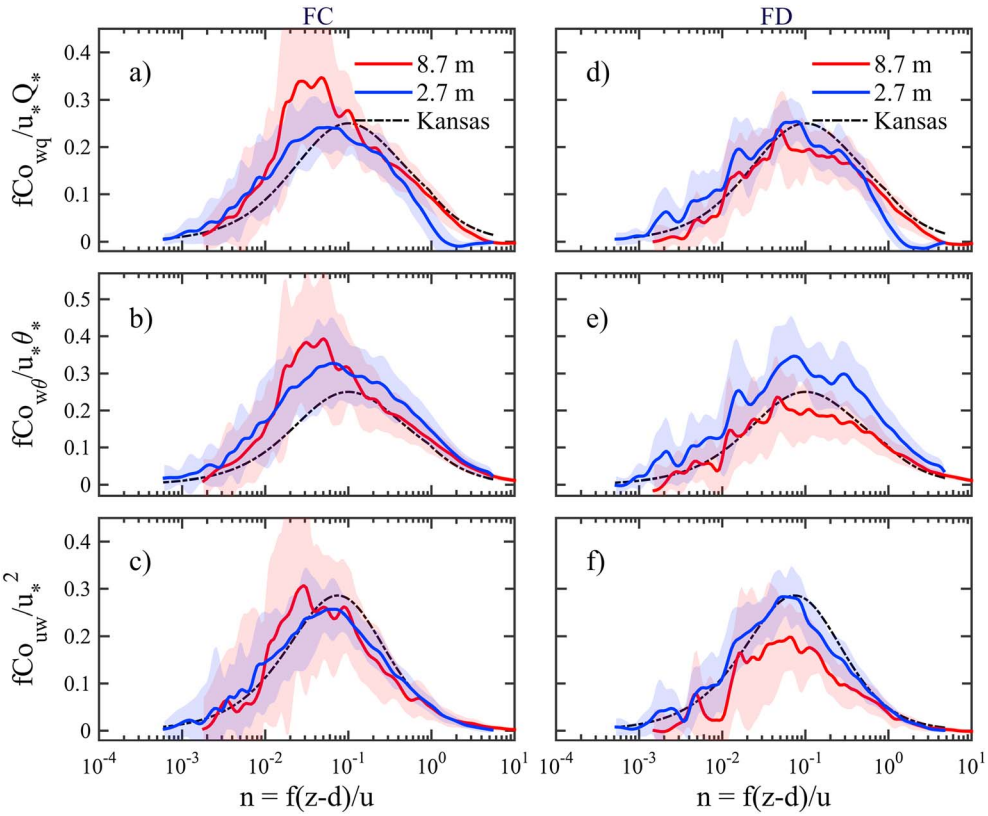

Figure 10. Like Figure 8 but for the normalized global wavelet cospectra of (a and d) *w*-*q*, (b and e) *w*-θ, and (c and f) *u*-*w*.

presence of the large eddies with the size of several hundred meters (i.e., 0.002 Hz $< f <$ 0.02 Hz) in the FC group, whereas the flux divergence was attributed to the depression or reduction of these large eddies in the FD group. In the next subsection, we will quantitatively analyze the contribution of the large eddies to turbulent transport using EEMD.

4.3.4. Quantitative Analysis of the Influence of Large Eddies on Flux Convergence/Divergence

EEMD is an objective method to decompose the time series into different IMF modes with dominant frequency scales. Since each IMF corresponds to a specific frequency, the variability of flux contribution from $IMF_{k,w}$ and $IMF_{k,c}$ as a function of k (k = 1, 2, 3, …, 14 for 30 min data with 10 Hz resolution) is similar to their flux cospectra as a function of natural frequency. Our cospectra did not show spectral gaps that could be used to split the time series into large eddies and small-scale turbulence. But when plotting the spectra and cospectra as a function of the natural frequency, the *u* and *v* spectra at 8.7 m were higher than that at 2.7 m in the low-frequency range ($f <$ 0.02 Hz) for the FC and FD groups. We considered the time series signals with frequency $f <$ 0.02 Hz as large eddies. The data were separated into two time series, one containing eddies with $f >$ 0.02 Hz (IMF_{1-9}), and one containing eddies with frequencies $f <$ 0.02 Hz (IMF_{10-14}). Flux contributions from IMF_{1-9} and IMF_{10-14} for the FC group and the FD group are presented in Table 3.

For the FC group, small-scale turbulence (i.e., IMF_{1-9}) contributes more to fluxes at 2.7 m than at 8.7 m, and $\overline{w'q'}$ at 2.7 m (0.093 $gm^{-2}s^{-1}$) was larger than that at 8.7 m (0.086 $gm^{-2}s^{-1}$). It was large eddies (i.e., IMF_{10-14}) that caused the flux convergence of *w*-*q* between 8.7 and 2.7 m since the flux contribution from these motions to $\overline{w'q'}$ at 8.7 m (0.068 $gm^{-2}s^{-1}$) was significantly (95% level) higher than that at 2.7 m (0.026 $g^{-2}s^{-1}$). Large eddies also contribute to $\overline{w'\theta'}$ and $\overline{w'u'}$ more at 8.7 m (0.024 kms^{-1} and $-0.026\,m^2s^{-2}$) than at 2.7 m (0.011 kms^{-1} and $-0.012\,m^2s^{-2}$), but the overall $\overline{w'\theta'}$ and $\overline{w'u'}$ presented divergence between 8.7 m and 2.7 m. For the FD group, flux contribution from large eddies at 8.7 m was larger than 2.7 m (e.g., 0.030 $gm^{-2}s^{-1}$ and 0.024 $gm^{-2}s^{-1}$ for $\overline{w'q'}$ at 8.7 and 2.7 m, respectively), but the increased amplitude was much smaller than that for the FC group. On the other hand, the decreased magnitude in flux contribution from small-scale

Table 3. Summary of Contribution to Fluxes ($\overline{w'q'}$, $\overline{w'\theta'}$, and $\overline{w'u'}$) From I (IMF_{1-9}) and II (IMF_{10-14}) at 8.7 and 2.7 m for Flux Convergence (FC) and Flux Divergence (FD) Under Unstable Conditions

		FC		FD	
		I	II	I	II
		Mean ± SD	Mean ± SD	Mean ± SD	Mean ± SD
$\overline{w'q'}$ ($gm^{-2}s^{-1}$)	**8.7 m**	0.086 ± 0.026	0.068 ± 0.026	0.072 ± 0.025	0.030 ± 0.014
	2.7 m	0.093 ± 0.027	0.026 ± 0.011	0.095 ± 0.034	0.024 ± 0.012
$\overline{w'\theta'}$ (kms^{-1})	**8.7 m**	0.035 ± 0.012	0.024 ± 0.011	0.025 ± 0.011	0.009 ± 0.007
	2.7 m	0.049 ± 0.014	0.011 ± 0.005	0.047 ± 0.015	0.009 ± 0.004
$\overline{w'u'}$ (m^2s^{-2})	**8.7 m**	−0.039 ± 0.017	−0.026 ± 0.015	−0.039 ± 0.017	−0.016 ± 0.012
	2.7 m	−0.052 ± 0.019	−0.012 ± 0.006	−0.069 ± 0.023	−0.012 ± 0.003

turbulence between two heights for the FD group (e.g., decrease in $\overline{w'q'}$ from 0.095 $gm^{-2}s^{-1}$ (2.7 m) to 0.072 $gm^{-2}s^{-1}$ (8.7 m)) was larger than that for the FC group. Therefore, the overall flux at 8.7 m was smaller than that at 2.7 m for the FD group.

5. Conclusions

Large eddies with different dominant sizes modulated turbulent structures and turbulent transport differently at 8.7 m and 2.7 m, producing the flux convergence (FC) and divergence (FD). For the FC group, large eddies with the size of several hundred meters (0.002 Hz $< f <$ 0.02 Hz) were more efficient than other sizes of large eddies in modulating turbulence structures. They enhanced the *w* spectra and contributed to the *w-q* cospectra over the low-frequency ranges more significantly at 8.7 m than at 2.7 m, leading to the FC in LE. For the FD group, however, these large eddies were depressed, leading to a significant decrease in the *w-q* cospectra at 8.7 m over the corresponding frequency ranges. Together with the divergence in the *w-q* cospectra over the rest of the frequency ranges, LE at 8.7 m was smaller than that at 2.7 m in the FD group. Our results indicate that these large eddies are active in enhancing the *w* spectra, distorting the scalar distribution, and modulating turbulent transport in the unstable ASL. Large eddies may increase or decrease eddy covariance fluxes, implying that the influence of large eddies on the surface energy balance closure can be both ways. In addition, it appears that the enhancement of *w* spectrum at low frequency is related to the ways of interaction between large eddies and local generated turbulence in the ASL. However, we did not observe a spectral gap or a consistent k^{-1} power law in our wind velocity components spectra, implying that our results cannot be fully explained by the available mechanisms (top-down and bottom-up turbulent models). Thus, further study is required to explore the underlying mechanisms that cause the difference between our (co) spectra and those reported in the literature.

Acknowledgments
We thank many participants for their assistance in the field. The National Science Foundation (NSF) provided funding for the deployment of NCAR facilities. Comments from three anonymous reviewers contributed to the improvement of this work. We acknowledge support by NSF AGS under grant 1112938. Zhongming Gao's work is sponsored by the China Scholarship Council (CSC) scholarship and NSF AGS 1112938. The data used in this study are available for free when requested to H.L.

References

Andreas, E. L. (1987), Spectral measurements in a disturbed boundary layer over snow, *J. Atmos. Sci.*, *44*(15), 1912–1939, doi:10.1175/1520-0469(1987)044<1912:SMIADB>2.0.CO;2.

Barnhart, B. L., W. E. Eichinger, and J. H. Prueger (2012), A new eddy-covariance method using empirical mode decomposition, *Boundary Layer Meteorol.*, *145*(2), 369–382, doi:10.1007/s10546-012-9741-6.

Charuchittipan, D., W. Babel, M. Mauder, J.-P. Leps, and T. Foken (2014), Extension of the averaging time in eddy-covariance measurements and its effect on the energy balance closure, *Boundary Layer Meteorol.*, *152*(3), 303–327, doi:10.1007/s10546-014-9922-6.

Farge, M. (1992), Wavelet transforms and their applications to turbulence, *Annu. Rev. Fluid Mech.*, *24*(1), 395–458, doi:10.1146/annurev.fl.24.010192.002143.

Foken, T. (2006), 50 years of the Monin-Obukhov similarity theory, *Boundary Layer Meteorol.*, *119*(3), 431–447, doi:10.1007/s10546-006-9048-6.

Foken, T. (2008), The energy balance closure problem: An overview, *Ecol. Appl.*, *18*(6), 1351–1367, doi:10.1890/06-0922.1.

Foken, T., M. Göockede, M. Mauder, L. Mahrt, B. Amiro, and W. Munger (2004), Post-field data quality control, in *Handbook of Micrometeorology: A Guide for Surface Flux Measurement and Analysis*, edited by X. Lee et al., pp. 181–208 , Kluwer, Dordrecht.

Gao, W., and B. L. Li (1993), Wavelet analysis of coherent structures at the atmosphere-forest interface, *J. Appl. Meteorol.*, *32*(11), 1717–1725, doi:10.1175/1520-0450(1993)032<1717:WAOCSA>2.0.CO;2.

Högström, U. (1990), Analysis of turbulence structure in the surface layer with a modified similarity formulation for near neutral conditions, *J. Atmos. Sci.*, *47*(16), 1949–1972, doi:10.1175/1520-0469(1990)047<1949:AOTSIT>2.0.CO;2.

Högström, U., J. C. R. Hunt, and A.-S. Smedman (2002), Theory and measurements for turbulence spectra and variances in the atmospheric neutral surface layer, *Boundary Layer Meteorol.*, *103*(1), 101–124, doi:10.1023/A:1014579828712.

Hong, J., T. Choi, H. Ishikawa, and J. Kim (2004), Turbulence structures in the near-neutral surface layer on the Tibetan Plateau, *Geophys. Res. Lett.*, *31*, L15106, doi:10.1029/2004GL019935.

Hong, J., J. Kim, H. Ishikawa, and Y. Ma (2010), Surface layer similarity in the nocturnal boundary layer: The application of Hilbert-Huang transform, *Biogeosciences*, *7*(4), 1271–1278, doi:10.5194/bg-7-1271-2010.

Horst, T. W., and D. H. Lenschow (2009), Attenuation of scalar fluxes measured with spatially-displaced sensors, *Boundary Layer Meteorol.*, *130*(2), 275–300, doi:10.1007/s10546-008-9348-0.

Huang, J., et al. (2008), An overview of the semi-arid climate and environment research observatory over the Loess Plateau, *Adv. Atmos. Sci.*, *25*(6), 906–921, doi:10.1007/s00376-008-0906-7.

Huang, J., X. Lee, and E. Patton (2009), Dissimilarity of scalar transport in the convective boundary layer in inhomogeneous landscapes, *Boundary Layer Meteorol.*, *130*(3), 327–345, doi:10.1007/s10546-009-9356-8.

Huang, N. E., and Z. Wu (2008), A review on Hilbert-Huang transform: Method and its applications to geophysical studies, *Rev. Geophys.*, *46*, RG2006, doi:10.1029/2007RG000228.

Huang, N. E., Z. Shen, S. R. Long, M. C. Wu, H. H. Shih, Q. Zheng, N.-C. Yen, C. C. Tung, and H. H. Liu (1998), The empirical mode decomposition and the Hilbert spectrum for nonlinear and non-stationary time series analysis, *Proc. R. Soc. A*, *454*(1971), 903–995.

Hudgins, L., C. A. Friehe, and M. E. Mayer (1993), Wavelet transforms and atmospheric turbulence, *Phys. Rev. Lett.*, *71*(20), 3279–3282.

Kaimal, J. C., and J. J. Finnigan (1994), *Atmospheric Boundary Layer Flows: Their Structure and Measurement*, Oxford Univ. Press, New York.

Kaimal, J. C., J. C. Wyngaard, Y. Izumi, and O. R. Coté (1972), Spectral characteristics of surface-layer turbulence, *Q. J. R. Meteorol. Soc.*, *98*(417), 563–589, doi:10.1002/qj.49709841707.

Katul, G. G., C.-T. Lai, K. Schäfer, B. Vidakovic, J. Albertson, D. Ellsworth, and R. Oren (2001), Multiscale analysis of vegetation surface fluxes: From seconds to years, *Adv. Water Resour.*, *24*(9–10), 1119–1132, doi:10.1016/S0309-1708(01)00029-X.

Katul, G. G., A. Sempreviva, and D. Cava (2008), The temperature-humidity covariance in the marine surface layer: A one-dimensiona1l analytical model, *Boundary Layer Meteorol.*, *126*(2), 263–278, doi:10.1007/s10546-007-9236-z.

Liu, H., G. Peters, and T. Foken (2001), New equations for sonic temperature variance and buoyancy heat flux with an omnidirectional sonic anemometer, *Boundary Layer Meteorol.*, *100*(3), 459–468.

Mauder, M., S. P. Oncley, R. Vogt, T. Weidinger, L. Ribeiro, C. Bernhofer, T. Foken, W. Kohsiek, H. A. R. De Bruin, and H. Liu (2007), The energy balance experiment EBEX-2000. Part II: Intercomparison of eddy-covariance sensors and post-field data processing methods, *Boundary Layer Meteorol.*, *123*(1), 29–54, doi:10.1007/s10546-006-9139-4.

McNaughton, K. G. (2004a), Attached eddies and production spectra in the atmospheric logarithmic layer, *Boundary Layer Meteorol.*, *111*(1), 1–18, doi:10.1023/B:BOUN.0000010997.51745.0f.

McNaughton, K. G. (2004b), Turbulence structure of the unstable atmospheric surface layer and transition to the outer layer, *Boundary Layer Meteorol.*, *112*(2), 199–221, doi:10.1023/B:BOUN.0000027906.28627.49.

McNaughton, K. G., and Y. Brunet (2002), Townsend's hypothesis, coherent structures and Monin-Obukhov similarity, *Boundary Layer Meteorol.*, *102*(2), 161–175, doi:10.1023/A:1013171312407.

McNaughton, K. G., and J. Laubach (1998), Unsteadiness as a cause of non-equality of eddy diffusivities for heat and vapour at the base of an advective inversion, *Boundary Layer Meteorol.*, *88*(3), 479–504, doi:10.1023/A:1001573521304.

McNaughton, K. G., and J. Laubach (2000), Power spectra and cospectra for wind and scalars in a disturbed surface layer at the base of an advective inversion, *Boundary Layer Meteorol.*, *96*(1-2), 143–185, doi:10.1023/A:1002477120507.

Monin, A. S., and A. M. Obukhov (1954), Basic laws of turbulent mixing in the surface layer of the atmosphere, *Tr. Akad. Nauk SSSR Geophiz. Inst.*, *24*(151), 163–187.

Oncley, S. P., C. A. Friehe, J. C. Larue, J. A. Businger, E. C. Itsweire, and S. S. Chang (1996), Surface-layer fluxes, profiles, and turbulence measurements over uniform terrain under near-neutral conditions, *J. Atmos. Sci.*, *53*(7), 1029–1044, doi:10.1175/1520-0469(1996)053<1029:SLFPAT>2.0.CO;2.

Oncley, S. P., et al. (2007), The energy balance experiment EBEX-2000. Part I: Overview and energy balance, *Boundary Layer Meteorol.*, *123*(1), 1–28, doi:10.1007/s10546-007-9161-1.

Ruppert, J., C. Thomas, and T. Foken (2006), Scalar similarity for relaxed eddy accumulation methods, *Boundary Layer Meteorol.*, *120*(1), 39–63, doi:10.1007/s10546-005-9043-3.

Schotanus, P., F. T. M. Nieuwstadt, and H. A. R. De Bruin (1983), Temperature measurement with a sonic anemometer and its application to heat and moisture fluxes, *Boundary Layer Meteorol.*, *26*(1), 81–93, doi:10.1007/BF00164332.

Smedman, A.-S., U. Högström, J. C. R. Hunt, and E. Sahlée (2007), Heat/mass transfer in the slightly unstable atmospheric surface layer, *Q. J. R. Meteorol. Soc.*, *133*(622), 37–51, doi:10.1002/QJ.7.

Stull, R. B. (1988), *An Introduction to Boundary Layer Meteorology*, Kluwer Acad., Dordrecht, Netherlands.

Sun, J., S. P. Burns, A. C. Delany, S. P. Oncley, T. W. Horst, and D. H. Lenschow (2003), Heat balance in the nocturnal boundary layer during CASES-99, *J. Appl. Meteorol.*, *42*(11), 1649–1666, doi:10.1175/1520-0450(2003)042<1649:HBITNB>2.0.CO;2.

Tanner, B. D., E. Swiatek, and J. P. Greene (1993), Density fluctuations and use of the krypton hygrometer in surface flux measurements, in *Management of Irrigation and Drainage Systems: Integrated Perspectives*, edited by R. G. Allen, pp. 945–952 , Am. Soc. Civil Eng., New York.

Torrence, C., and G. P. Compo (1998), A practical guide to wavelet analysis, *Bull. Am. Meteorol. Soc.*, *79*(1), 61–78, doi:10.1175/1520-0477(1998)079<0061:APGTWA>2.0.CO;2.

von Randow, C., B. Kruijt, and A. A. M. Holtslag (2006), Low-frequency modulation of the atmospheric surface layer over Amazonian rain forest and its implication for similarity relationships, *Agric. For. Meteorol.*, *141*(2–4), 192–207, doi:10.1016/j.agrformet.2006.10.005.

Wang, G., J. Huang, W. Guo, J. Zuo, J. Wang, J. Bi, Z. Huang, and J. Shi (2010), Observation analysis of land-atmosphere interactions over the Loess Plateau of northwest China, *J. Geophys. Res.*, *115*, D00K17, doi:10.1029/2009JD013372.

Wang, J., J. Song, Y. Huang, and C. Fan (2013), Application of the Hilbert-Huang transform to the estimation of air-sea turbulent fluxes, *Boundary Layer Meteorol.*, *147*(3), 553–568, doi:10.1007/s10546-012-9784-8.

Webb, E. K., G. I. Pearman, and R. Leuning (1980), Correction of flux measurements for density effects due to heat and water vapour transfer, *Q. J. R. Meteorol. Soc.*, *106*(447), 85–100, doi:10.1002/qj.49710644707.

Wu, Z., and N. E. Huang (2009), Ensemble empirical mode decomposition: A noise-assisted data analysis method, *Adv. Adapt. Data Anal.*, *01*(01), 1–41, doi:10.1142/S1793536909000047.

Zermeño-Gonzalez, A., and L. E. Hipps (1997), Downwind evolution of surface fluxes over a vegetated surface during local advection of heat and saturation deficit, *J. Hydrol.*, *192*(1–4), 189–210, doi:10.1016/S0022-1694(96)03108-3.

Zhang, Y., H. Liu, T. Foken, Q. Williams, S. Liu, M. Mauder, and C. Liebethal (2010), Turbulence spectra and cospectra under the influence of large Eddies in the Energy Balance EXperiment (EBEX), *Boundary Layer Meteorol.*, *136*(2), 235–251, doi:10.1007/s10546-010-9504-1.

Zhang, Y., H. Liu, T. Foken, Q. Williams, M. Mauder, and C. Thomas (2011), Coherent structures and flux contribution over an inhomogeneously irrigated cotton field, *Theor. Appl. Climatol.*, *103*(1-2), 119–131, doi:10.1007/s00704-010-0287-6.